

Comparison of Digital Demodulation Algorithms for LVDT Sensors in Circuits with Lightning Protection

Marcos A. O. Campos Filho, MC
Instituto Tecnológico de Aeronáutica
marcos.filho@embraer.com.br

Prof. Luiz Carlos Sandoval Góes
Instituto Tecnológico de Aeronáutica
goes@ita.br

Raphael das Neves Calvo, MC
EMBRAER
raphael.calvo@embraer.com.br

Abstract—The implementation of digital Control Systems can bring several advantages to aircraft manufacturers including improvement in reliability and increased tolerance to environmental conditions such as temperature and electrical noise.

A Simulink model for a digital position acquisition system for aircraft primary control surfaces is presented, comprised by a Linear Variable Differential Transformer (LVDT) as displacement sensor, a protective passive filter for lightning induced transients, an Analog-to-Digital converter and a digital demodulation system.

This work performs an implementation and comparison of two strategies: the Peak Detector, based on the instant amplitude of the signal and the Oversampling/Averaging, based on the mean value of the signal over a time window.

I. INTRODUCTION

The main objective of this work is to evaluate the performance of two digital algorithms, Peak Detector and Oversampling/Averaging to demodulate the output of an LVDT, utilized as positioning sensor on an electro-hydraulic actuator. The constructed position acquisition system will then be integrated to the electro-hydraulic actuator model developed in [1] and the composite model will serve as platform to analyse both strategies under the following aspects:

- 1) Steady state error for a step input;
- 2) Effect of number of sampled points per cycle;
- 3) Tolerance to noise on input.

II. MODEL CONSTRUCTION

A. Linear Variable Differential Transformer

This section presents the implementation of an 6-wire Linear Variable Differential Transformer (LVDT) model using Simscape, a library to model physical systems within the Simulink environment. The custom behavioral model is described by a system of differential algebraic equations (DAEs) and was built using Simscape language [2]. The LVDT is comprised of three coils within which a magnetically permeable core moves to provide variable magnetic coupling between the primary coil and the secondary coils A and B. An equivalent circuit for the LVDT is presented in Figure 1, similar to one used by [3].

The values L_k and R_k are the self-inductance and resistance of the winding k (primary or secondaries A or B). Similarly, i_k denotes the current on winding k . M_{ap} and M_{bp} are the mutual inductances between the primary coil and each secondary, given by equation 1 [4].

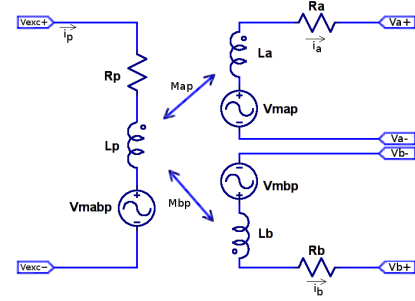


Fig. 1. LVDT equivalent circuit

$$\begin{aligned} M_{ap} &= k_a(t) \sqrt{L_a L_p} \\ M_{bp} &= k_b(t) \sqrt{L_b L_p} \end{aligned} \quad (1)$$

where values $k_a(t)$ and $k_b(t)$ are the *coupling coefficients*, varying in time. The voltages induced on each secondary are represented by V_{map} and V_{mbp} in Figure 1.

Considering two coils in the configuration shown in Figure 2, using Faraday's Law, it is possible to show that the voltage V induced in coil 2 due to I_1 and a time-varying coupling coefficient (and in consequence a time-varying mutual inductance $M(t)$) is given by equation 2.

$$V = \frac{dM(t)}{dt} I_1 + M(t) \frac{dI_1}{dt} \quad (2)$$

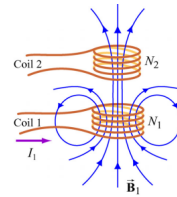


Fig. 2. Coupled coils - Source [5]

When the LVDT is totally retracted, the coupling coefficient k_a is K_{min} and k_b is K_{max} and when totally extended, the opposite. Since the variation is linear with core position $x(t)$ (normalized), the coupling coefficients can be expressed by equations 3.

$$\begin{aligned} k_a(t) &= \frac{K_{max} - K_{min}}{2}x(t) + \frac{K_{max} + K_{min}}{2} \\ k_b(t) &= \frac{-(K_{max} - K_{min})}{2}x(t) + \frac{K_{max} + K_{min}}{2} \end{aligned} \quad (3)$$

The Simscape expression for primary and secondary windings are given by equations 4 and 5 respectively. Suitable values for the simulation were obtained from typical values collected from multiple sources ([6], [7], [8]). The parameters for the model are summarized on Table I.

$$\begin{aligned} V_{exc} = & R_p i_p + L_p \frac{di_p}{dt} + \left(M_{ap} \frac{di_a}{dt} + i_a \frac{dM_{ap}}{dt} \right) \\ & + \left(M_{bp} \frac{di_b}{dt} + i_b \frac{dM_{bp}}{dt} \right) \end{aligned} \quad (4)$$

$$\begin{aligned} V_a = & R_a i_a + L_a \frac{di_a}{dt} + \left(M_{ap} \frac{di_p}{dt} + i_p \frac{dM_{ap}}{dt} \right) \\ V_b = & R_b i_b + L_b \frac{di_b}{dt} + \left(M_{bp} \frac{di_p}{dt} + i_p \frac{dM_{bp}}{dt} \right) \end{aligned} \quad (5)$$

TABLE I
LVDT PARAMETERS

Parameter	Value
Excitation voltage (V_{exc})	$7V_{RMS} @ 3kHz$
Primary inductance (L_p) / resistance (R_p)	$80mH / 200\Omega$
Secondary A inductance (L_a) / resistance (R_a)	$40mH / 150\Omega$
Secondary B inductance (L_b) / resistance (R_b)	$40mH / 150\Omega$
Coupling coefficients [K_{min} , K_{max}]	[0.178, 0.535]
Maximum absolute ratio (ratiometric demodulation)	0.5
Minimum signal voltage (full extended)	$0.873V_{RMS}$
Maximum signal voltage (full extended)	$2.625V_{RMS}$
Maximum phase	7.55°

B. Transient Filter

Aircraft manufacturers refer to RTCA/DO-160 Section 22 (Lightning Induced Transient Susceptibility) [9] as minimum requirements to design and test airborne equipment with standardized and representative waveforms for lightning induced transients. For a typical configuration where the actuator is installed in a non-pressurized region and its sensor interfaces and cabling passes through non-metallic (composite) regions, a pin injection test comprised of Waveforms 3 and 4 (Figure 3) at power level 3 [9] is indicated to verify the controller's susceptibility. A passive low pass filter was designed to attenuate the waveforms so the maximum output lies below 10V.

Detecting and handling these transients in the controller is out of the scope of this work so to speed up the simulation a simplified RC filter with similar frequency response around $3kHz$ was used, with cutoff frequency at $30kHz$. The filters parameters are summarized on Table II.

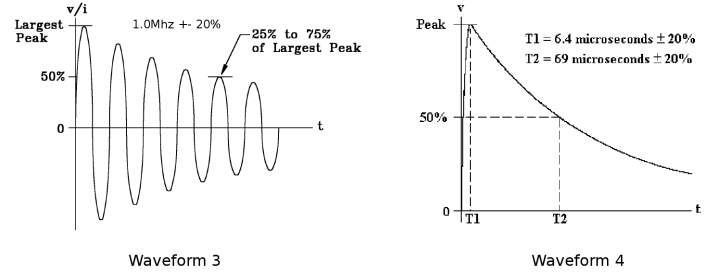


Fig. 3. Waveforms 3 and 4 - Source: [9]

TABLE II
RC LOW PASS FILTER PARAMETERS

Parameter	Unfiltered	Complete filter	Simplified filter
Magnitude @3kHz	-8.519dB	-4.549dB	-7.717dB
Phase @3kHz	7.554°	-11.37°	-0.66°

C. Range Converter

This circuit is used to match the signal range of the filter output to the input of the analog-to-digital converter. This step also makes possible to balance the attenuation caused by the previous filtering stage and serves as a high impedance load for the filter and a low impedance source for the ADC. [10] provides guiding to design a circuit capable of adding gain and DC offset to a signal, based on the desired input and output ranges (Table III).

TABLE III
RANGE CONVERTER MODEL PARAMETERS

Parameter	Value
Input signal range	[-4.50, 4.50]V
Output signal range	[0.02, 9.40]V
ADC range utilization	93.8%

D. Analog-to-Digital Converter

This section presents the behavioral model of a Successive Approximation Register (SAR) ADC which performance parameters were based on the Texas Instruments ADS8638, a 12-bit SAR ADC capable of measuring 8 time-multiplexed channels in multiple selectable ranges up to $\pm 10V$ at $1MSPS$. This device provides a sample-and-hold front-end with no latency in conversions and no missing codes [11].

1) *Input Stage*: The input stage of the ADC was modelled as a voltage meter across a large value resistor ($1M\Omega$) for each input, as shown on figure 4. The settling time of the ADS8638 is in the order of $250ns$, which is considered instantaneous given the simulation step time of $100ns$. It is also assumed that the output of the multiplexer is connected to a buffer with input resistance many times larger than the conduction resistance of each channel.

2) *Channel crosstalk and channel selection*: A square matrix with order equal to the number of channels is built as shown in 6, where CT_g is the channel crosstalk gain, extracted from datasheet. In order to simplify the implementation, it

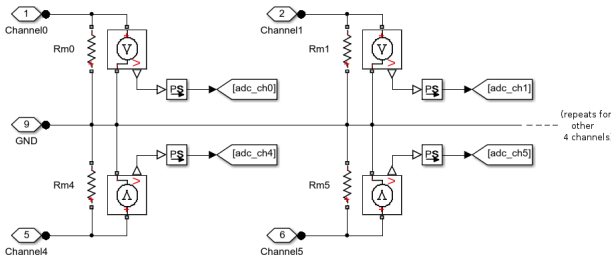


Fig. 4. ADC input stage

is considered that the crosstalk is the same for each pair of channels. The output is fed to a multiport switch that selects the appropriate channel.

$$\begin{bmatrix} \hat{V}_{Ch_0} \\ \hat{V}_{Ch_1} \\ \vdots \\ \hat{V}_{Ch_{n-1}} \end{bmatrix} = \begin{bmatrix} 1 & CT_g & \cdots & CT_g \\ CT_g & 1 & \cdots & CT_g \\ \vdots & \vdots & \ddots & \vdots \\ CT_g & CT_g & \cdots & 1 \end{bmatrix} \begin{bmatrix} V_{Ch_0} \\ V_{Ch_1} \\ \vdots \\ V_{Ch_{n-1}} \end{bmatrix} \quad (6)$$

3) *Harmonic distortion*: Harmonic distortion is artificially created in a scheme similar to one used in [12], consisting in taking the input signal and applying a non linear function (Figure 5). The harmonics are created according to 7 and a gain for each signal is adjusted to approximate the desired Total Harmonic Distortion (THD).

$$\begin{aligned} \sin^2(\omega t) &= \frac{1}{2}(1 - \cos(2\omega t)) \\ \sin^3(\omega t) &= \frac{1}{4}(3\sin(\omega t) - \sin(3\omega t)) \\ \sin^4(\omega t) &= \frac{1}{8}(-4\cos(2\omega t) + \cos(4\omega t) + 3) \end{aligned} \quad (7)$$

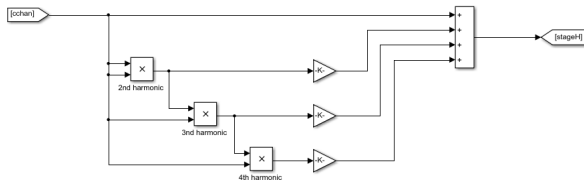


Fig. 5. Harmonic distortion

4) *Gain, offset and internal noise*: The final stage before quantization inserts the gain error, the offset error and adds the internal noise, modelled as a Band-Limited White Noise block. All quantities are specified in *LSB* units and the implementation is straightforward, shown in figure 6.

5) *Quantizer*: The strategy adopted uses a lookup table (LUT) block with interpolation disabled so the voltage read in sampling instant kT_s is rounded to the nearest code. In the case of a SAR ADC, the comparator and the feedback DAC are the most significant error sources affecting code transition levels [13], caused by inaccuracies of the weight values for each bit b_i for $i = 1, 2, \dots, N$, where N is ADC resolution.

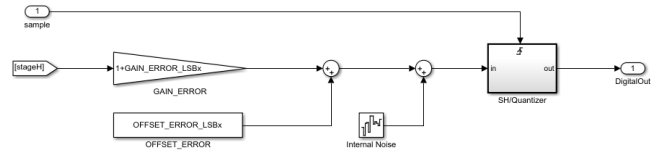


Fig. 6. Gain and offset errors and internal noise

To generate the periodic behavior on INL, the INL vector is initialized with a sine function with low frequency (equation 8). The function is evaluated for $k = 1 : 2^N - 1$. A weight value W_0 can be used and in this case $W_0 = 1$. For N steps, a sine with double the frequency of the previous one is added to the INL vector. The obtained vector is normalized, a small amount of noise is added it is then scaled to comply with minimum and maximum values from datasheet. Since INL is found by computing the cumulative sum of DNL (equation 9), to obtain DNL the opposite operation was used (equation 10).

$$INL_0 = W_0 * \sin\left(2\pi \frac{k}{2^N - 1}\right)$$

$$INL = \sum_{n=1}^{N-1} \left(INL_{n-1} + W_n * \sin\left(2^{n+1}\pi \frac{k}{2^N - 1}\right) \right) \quad (8)$$

$$INL_k = \sum_{i=1}^{k-1} DNL_i \quad (9)$$

$$DNL_k = INL_{k+1} - INL_k \quad (10)$$

The obtained DNL and INL values are shown on figure 7 and the values from ADS8638 datasheet are show on figure 8. The model dynamic performance parameters are summarized on table IV.

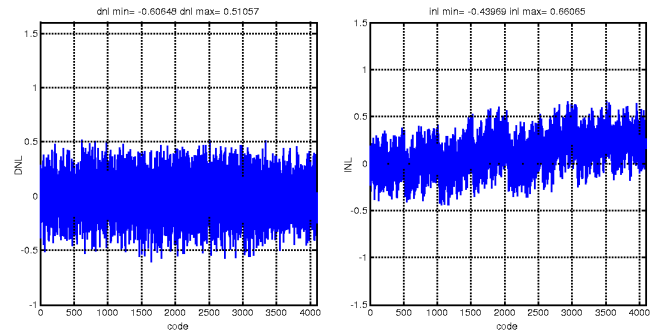


Fig. 7. Generated DNL and INL values

III. DEMODULATION ALGORITHMS

To demodulate the signal and compute the position, an LVDT of adequate range must be selected. From [1], the excursion of the piston rod is $\pm 3.74in$ ($\pm 95mm$). For an LVDT with stroke range of $\pm 4in$ ($101.6mm$) this would be about 94% of the excursion leaving a small mechanical

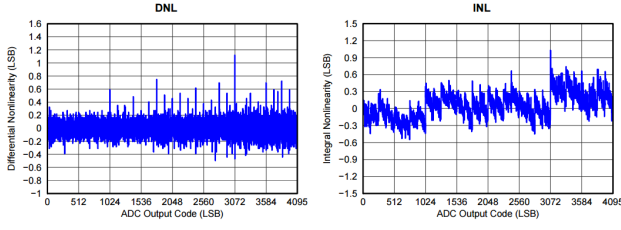


Fig. 8. Real DNL and INL values for ADS8638 - Source: [11]

TABLE IV
ADC MODEL DYNAMIC PERFORMANCE PARAMETERS

Parameter	Real value	Model value
Signal-to-Noise ratio (SNR)	71.8dB	72.2dB
Total harmonic distortion (THD)	-81dB	-81.05dB
Signal-to-Noise-and-Distortion ratio (SINAD)	71.3dB	71.6dB
Spurious-free dynamic range (SFDR)	-83dB	-82dB
Effective number of bits (ENOB)	11.55	11.61

tolerance. Thus, an LVDT with stroke range equal to $\pm 5in$ (127mm) is selected and the rod excursion is 74.8%. By convention, L is the actuator length, known as pin-to-pin distance, R is the horn radius and C is the distance between the anchorage point in the non-moveable surface and the anchorage point in the control surface, defining the RLC triangle (Figure 9) [1].

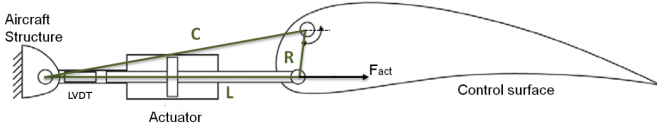


Fig. 9. Actuator, LVDT, surface and RLC triangle - Source: [1] (modified)

The variable being acquired is the piston rod position and the controlled one is the surface deflection, against which the performance of the algorithms will be evaluated. The relation between those variables is given by equation 11, where x_p is the current piston rod displacement, θ_s is the surface deflection and β_0 is the angle \widehat{RC} while surface is in neutral position.

$$\theta_s = \arccos\left(\frac{R^2 + C^2 - (L_0 + x_p)^2}{2RC}\right) - \beta_0 \quad (11)$$

A. Peak Detector

To obtain the peak value, the following procedure is used. The input vectors \hat{V}_a and \hat{V}_b are the signals from channel A and channel B respectively.

- 1) The offset value V_{off} is obtained (output of the range converter when the input is zero);
- 2) V_{off} is subtracted from both vectors and the absolute value is taken, effectively rectifying the signals;
- 3) The algorithm on Figure 10 is applied to obtain the mean peak value, where Z_{xt} is the zero crossing threshold and Z_c is the counted number of samples below the threshold. The rightmost peak from each channel is

discarded preventing incomplete half waves to interfere with result (Figure 11);

- 4) The mean peak values $\hat{V}_{a_{out}}$ and $\hat{V}_{b_{out}}$ are applied on equation 12 to obtain the current ratio $r_{computed}$ and then the position. For a maximum stroke (S_{max}) of 5in, the maximum ratio (r_{max}) would be 0.5.

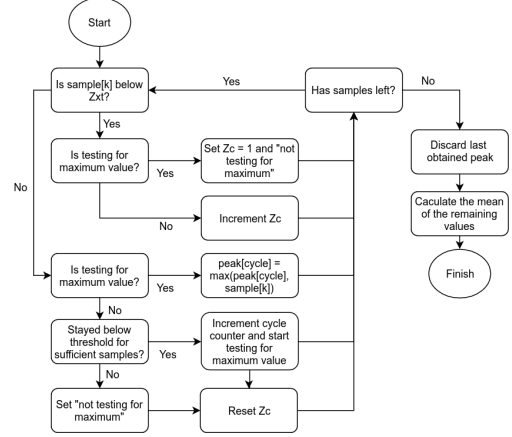


Fig. 10. Peak detection algorithm

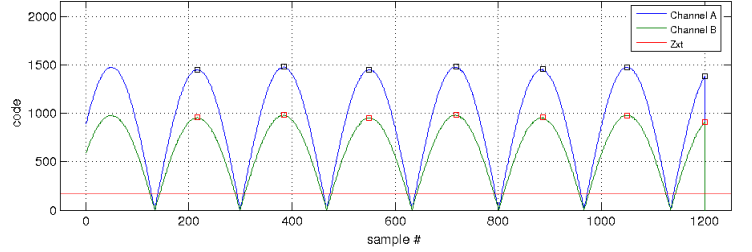


Fig. 11. Detected peaks

$$r_{computed} = \frac{\hat{V}_{a_{out}} - \hat{V}_{b_{out}}}{\hat{V}_{a_{out}} + \hat{V}_{b_{out}}} \quad (12)$$

$$x_{p_{computed}} = \frac{r_{computed}}{r_{max}} S_{max}$$

B. Oversampling/Averaging

Oversampling and averaging can be used to increase measurement resolution, without using a high resolution ADC. The technique improves the SNR (when white noise is concerned) and resolution at the cost of increased CPU utilization and lower throughput. To obtain the average value of the signal, the following procedure is used:

- 1) Similarly to peak detector algorithm, the signal is rectified by subtracting V_{off} and taking the absolute value;
- 2) The first and the last zero crossings are obtained from the sampled signal delimiting a integer number of half-cycles. The points between the zero crossings are averaged for each channel;
- 3) The average values $\hat{V}_{a_{out}}$ and $\hat{V}_{b_{out}}$ are applied on equation 12 to obtain the current ratio $r_{computed}$ and then the position.

IV. EXPERIMENTS

A. Steady State Error

This experiment verifies the steady state error for a step input of 30° for each algorithm in the absence of external influence. In this tests, no noise was inserted on the signal path besides the internal noise from the ADC. The gain and offset errors, correctable via calibration, are set to zero. The results are shown on Figures 12 and are summarized on table V.

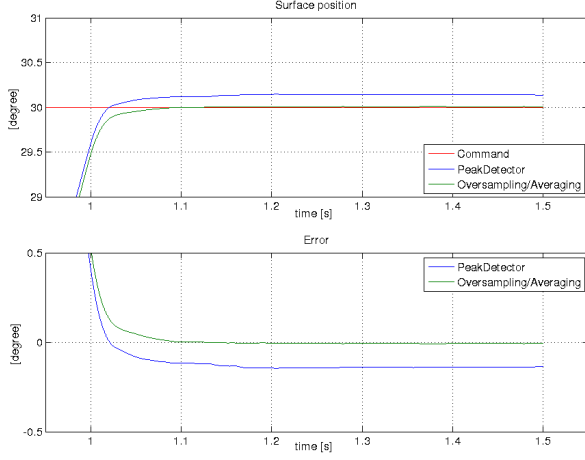


Fig. 12. Step response for both algorithms in the absence of external error (zoom)

TABLE V
STEP INPUT RESPONSE

Parameter	Expected	Peak Detector	Oversampling
Steady state value [$^\circ$]	30.00	30.14	30.01
Steady state error [%]	< 1.00	0.46	0.02
Settling time (1%) [s]	-	0.802	0.806

B. Effect of number of sampled points per cycle

This experiment characterizes the influence the number of sampled points on each half wave in the step response of the system. Effectively, changing the number of the points is equivalent to sample at a lower frequency. To verify this effects, a point will be taken every given number of points N before processing, as described by table VI.

TABLE VI
NUMBER OF USED POINTS

Rule	Number of points	Effective sampling frequency
1/1	166	1000 <i>kSPS</i> (default)
1/2	83	500 <i>kSPS</i>
1/4	41	250 <i>kSPS</i>
1/8	20	125 <i>kSPS</i>

C. Tolerance to noise on input

The following tests are intended to verify the tolerance of both algorithms to a noisy input. The same white noise signal

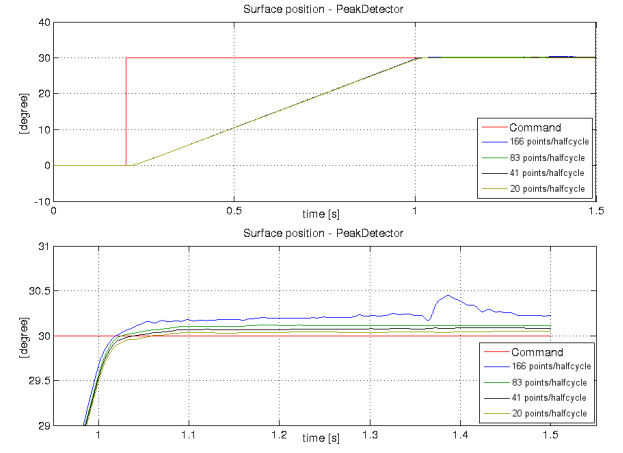


Fig. 13. Effect of the number of samples on the Peak Detector algorithm

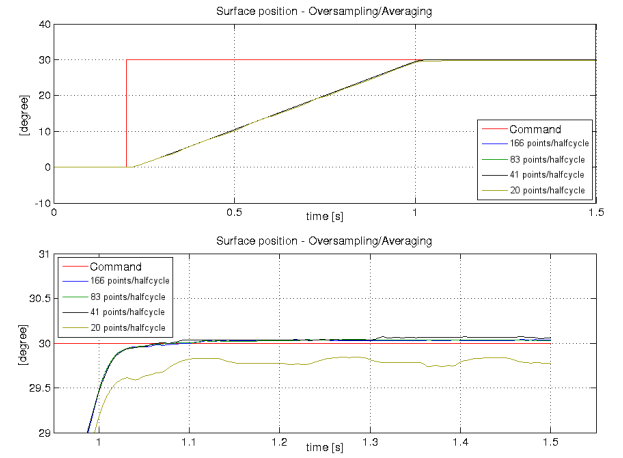


Fig. 14. Effect of the number of samples on the Oversampling/Averaging algorithm

TABLE VII
STEP INPUT RESPONSE - PEAK DETECTOR

Parameter	Expected	Samples per half-cycle			
		166	83	41	20
Steady state value [$^\circ$]	30.00	30.22	30.11	30.08	30.05
Steady state error [%]	< 1.00	0.75	0.37	0.27	0.16
Settling time (1%) [s]	-	1.218	0.802	0.804	0.805

TABLE VIII
STEP INPUT RESPONSE - OVERSAMPLING/AVERAGING

Parameter	Expected	Samples per half-cycle			
		166	83	41	20
Steady state value [$^\circ$]	30.00	30.04	30.03	30.06	29.78
Steady state error [%]	< 1.00	0.12	0.10	0.18	-0.74
Settling time (1%) [s]	-	0.807	0.806	0.808	0.873

is injected into both channels through independent current sources on each channel. The results are shown in Figures 15 and 16 and are summarized on tables IX and X.

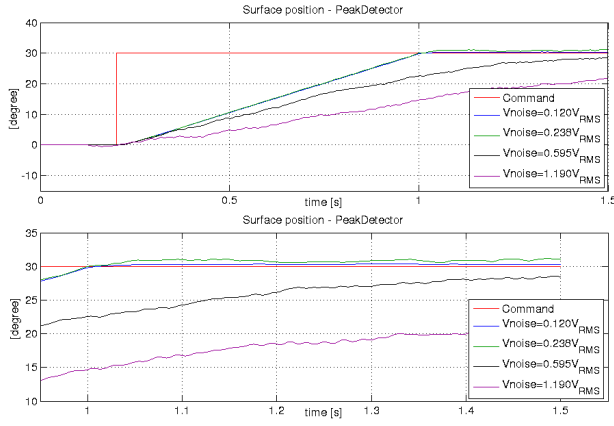


Fig. 15. Effect of input noise on the Peak Detector algorithm

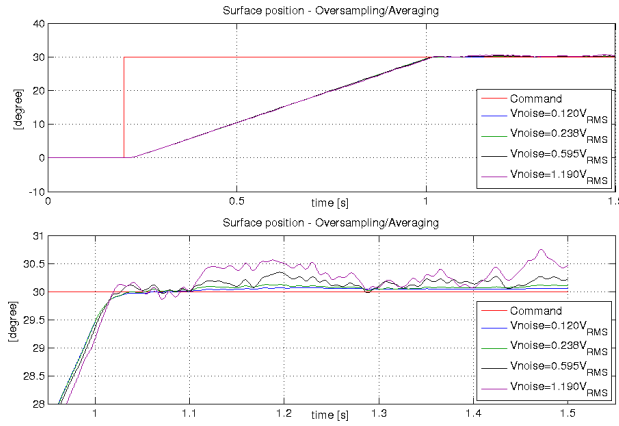


Fig. 16. Effect of input noise on the Oversampling/Averaging algorithm

TABLE IX
STEP INPUT RESPONSE - PEAK DETECTOR

Parameter	Expected	V_{noise} [V_{RMS}]			
		0.120	0.238	0.595	1.120
Steady state value [°]	30.00	30.28	31.05	28.50	21.83
Steady state error [%]	< 1.00	0.92	3.51	-5.02	-27.2
Settling time (1%)	-	1.23	—	—	—

TABLE X
STEP INPUT RESPONSE - OVERSAMPLING/AVERAGING

Parameter	Expected	V_{noise} [V_{RMS}]			
		0.120	0.238	0.595	1.120
Steady state value [°]	30.00	30.06	30.11	30.22	30.46
Steady state error [%]	< 1.00	0.19	0.36	0.74	1.55
Settling time (1%) [s]	-	0.81	0.81	1.00	—

V. CONCLUSION

The position acquisition system was successfully modelled and integrated to the electro-hydraulic actuator model developed by [1] and the control loop was successfully closed with both demodulation strategies.

In order to evaluate the performance of the demodulation algorithms regarding steady state error, an experiment was set up minimizing the external error sources (no noise on

LVDT, null gain and offset errors on ADC) and was observed that the Peak Detector responded faster, reaching the setpoint first but also presented a steady state error larger than the Oversampling/Averaging.

Regarding the variation of the number of samples, a low noise test setup caused the Peak Detector performance to improve when the number of points was reduced, since this was effectively smoothing the signal. The performance of Oversampling/Averaging degraded with reduction of the number of points reaching a steady state error greater than Peak Detector when using only 1/8 of points. Once the noise was increased Oversampling/Averaging outperformed the Peak Detector, suggesting a higher susceptibility to noise on the latter.

The results from the noise level test confirmed that Oversampling/Averaging is more robust, being capable of resolving the rod position even with noise levels as high as $0.6V_{RMS}$ without violating the steady state error requirement of 1%. At noise levels as low as $0.120V_{RMS}$ the Peak Detector produced a steady state error of 0.924%, almost reaching the limit above mentioned.

REFERENCES

- [1] H. M. S. BALLESTEROS, "Dynamic stiffness enhancement of a flight control actuator using control techniques," Master in Engineering, ITA, São José dos Campos, 2015.
- [2] MathWorks. (2016) Typical simscape language tasks. Accessed on: 2017/01/30. [Online]. Available: <https://www.mathworks.com/help/physmod/simscape/lang/typical-simscape-language-tasks.html>
- [3] R. P. F. DIAS, "Transformador diferencial de variação linear - condicionamento de sinal e desmodulação síncrona," Master in Engineering, Instituto Superior de Engenharia de Lisboa, 2015.
- [4] Electronics Tutorials. (2016) Mutual inductance. Accessed on: 2016/09/19. [Online]. Available: <http://www.electronics-tutorials.ws/inductor/mutual-inductance.html>
- [5] B. Knuteson, G. Stephans, J. Belcher, J. Joannopolus, M. Feld, and P. Dourmashkin. (2005) Inductance and magnetic energy. Accessed on: 2017/03/18. [Online]. Available: <http://web.mit.edu/viz/EM/visualizations/coursenotes/modules/guide11.pdf>
- [6] TE Connectivity. (2017) Linear position sensors - lvdlt/lvit - heavy duty gage head. Accessed on: 2017/02/05. [Online]. Available: <http://www.te.com/usa-en/product-CAT-LVDT0041.html>
- [7] Althen. (2017) M-12 schaevitz layer-wound lvdlt. Accessed on: 2016/12/10. [Online]. Available: http://www.althensensors.com/displacement_and_position_sensors/m12/
- [8] Active Sensors. (2017) Lvdlt position sensors. Accessed on: 2017/02/05. [Online]. Available: <http://www.activesensors.com/products/lvdt-position-sensors>
- [9] RADIO TECHNICAL COMMISSION FOR AERONAUTICS. (2010) DO-160G. Environmental Conditions and Test Procedures for Airborne Equipment.
- [10] Texas Instruments. (2002) Designing gain and offset in thirty seconds. Accessed on: 2016/10/06. [Online]. Available: <http://www.ti.com/lit/an/sloa097/sloa097.pdf>
- [11] —. (2017) 12-bit, 8-channel, bipolar sar with software selectable input ranges. Accessed on: 2016/11/12. [Online]. Available: <http://www.ti.com/product/ADS8638>
- [12] S. M. Taheri and B. Mohammadi, "Behavioral modeling of typical non-ideal analog to digital converter using matlab," *TMLAI - Transactions on Machine Learning and Artificial Intelligence*, 2014.
- [13] L. Michaeli, J. Saliga, and P. Michalko, "Unified adc nonlinearity error model for sar adc," *Journal of the International Measurement Confederation*, 2006.